Hindawi
Complexity
Volume 2018, Article ID 7130532, 17 pages
https://doi.org/10.1155/2018/7130532

*Research Article*

# Complexity Analysis on the Aerodynamic Performance of the Mega High-Speed Train Caused by the Wind Barrier on the Embankment

**He-xuan Hu**,[1,2] **Wan-xin Lei**,[3] **and Ye Zhang**[1]

[1]*College of Computer and Information, Hohai University, Nanjing 211100, China*
[2]*Department of Electrical Engineering, Tibet Agricultural and Animal Husbandry College, Lin-zhi, Tibet 860000, China*
[3]*School of Public Administration, Hohai University, Nanjing 211100, China*

Correspondence should be addressed to Ye Zhang; yzh@hhu.edu.cn

Received 18 April 2018; Revised 19 May 2018; Accepted 29 May 2018; Published 12 July 2018

Academic Editor: Changzhi Wu



With the world development of high-speed railways and increasing speeds, aerodynamic forces and moments acting on trains have been increased further, making trains stay at a "floated" state. Under a strong crosswind, the aerodynamic performance of a train on the embankment is greatly deteriorated; lift force and horizontal force borne by trains will be increased quickly; trains may suffer derailing or overturning more easily compared with the flat ground; train derailing will take place when the case is serious. All of these phenomena have brought risks to people's life and properties. Hence, the paper establishes an aerodynamic model about a high-speed train passing an air barrier, computes aerodynamic forces and moments, and analyzes pulsating pressures on the train surface as well as those of unsteady flow fields around the train. Computational results indicate that when the train passed the embankment air barrier, the head wave of air pressure full wave is more than the tail wave; the absolute value of negative wave is more than that of the positive wave, which is more obvious in the head train. When the train is passing the air barrier, pressure pulsation values at head train points are more than those at other points, while pressure changes most violently at the train bottom, and pressure values close to the air barrier are more than those points far from the air barrier. Pressure values at the cross section 1 were larger than those of other points. Pressure values at measurement points of the tail train ranked the second place, with the maximum negative pressure of 1253 Pa. Pressure change amplitudes and maximum negative pressure on the train surface are increased quickly, while pressure peak values on the high-speed train surface are in direct ratio to the running speed. With the increased speed of the high-speed train, when it is running in the embankment air barrier, the aerodynamic force and moment borne by each train body are increased sharply, while the head train suffers the most obvious influences of aerodynamic effects.

## 1. Introduction

With the increase of the train speed, the high-speed running of a train will motivate motion of air around the train. Hence, a specific unsteady flow field can be generated, which is generally called "train wind" [1]. The disturbance train wind generated by a train to the surrounding environment will lead to changes in air pressure and flowing. Train wind will act on people and objects near a railway, which can bring serious safety risks to roadside workers and passengers on the platform. Meanwhile, objects beside a railway may be rolled up or blown away. In addition, high running speed may cause huge damage of equipment and buildings beside a railway. Influencing intensity of train wind on railways mainly depends on the train running speed, distance from the train side walls, railway environmental conditions, train appearance, and other factors. Platform safety distance and operation safety distance are determined based on the train wind research [2].

In wind regions, strong wind will be prohibited by the embankment and thus accelerating effect will take place on the embankment [3]. The higher embankment suffers more

obvious accelerating effect. Survey results of historical accidents taking place on the Lanzhou-Xinjiang railway line indicate that all the accidents took place on embankment sections [4].

In order to prevent train accidents, a lot of researches have been conducted to the strong wind, where wind-shielding walls are generally taken as the protection measure [5–11]. Fujii et al. described Japanese accidents caused by train wind as well as strong-wind countermeasures and mentioned that wind-shielding gates with certain ventilation rates can effectively enhance train stability under crosswind, but these researches failed to analyze wind speeds of the overhead line system after installation of the wind-shielding gates [5]. Zhang and Liu optimized slope angles of earth-embankment wind-shielding walls on the Chinese Xinjiang single line, but such wind-shielding wall occupies a large area. These researches failed to analyze wind speeds of overhead lines after installation of the wind-shielding walls [6]. Lin introduced bridge wind-prevention construction technologies applied in 100 km wind zone of Xinjiang, China, and summarized the constitution and installation of bridge wind-shielding walls (steel-plate type), but it is not applicable to passenger transport lines in the wind area [8]. Gao and Duan used two-dimensional models to research influences brought by single-sided and double-sided wind-shielding walls with different heights on the single line to aerodynamic performance of trains, but the research results could not reflect three-dimensional effects of flow fields around rain bodies. Plus, the boxcar was selected in the research, while influences of wind-shielding walls on wind speeds of overhead lines were not described [12]. Li et al. conducted optimized simulation of appearance of open-hole wind-shielding walls on high-speed railways located at the embankment, obtaining influences brought by factors such as hole shape, hole layout mode, aperture ratio, and hole diameter to aerodynamic performance of the D-series high-speed train. However, structural form, installation mode, position, height, and other properties of the wind-shielding wall structure may not be applicable to bridges on the passenger transport lines (high-speed railways) in wind areas. Plus, influences brought by the height of the wind-shielding wall to overhead line wind speed were not taken into account [13]. In [14, 15], the rational height of the wind-shielding wall on the Lanzhou-Xinjiang railway line was researched based on the principle of minimizing the overturning moment coefficient sum of vehicles on first and second vehicle lines. Reference [16] introduces wind-shielding performance of wind-shielding walls of earth embankment type, reinforced earth type, concrete pillow direct-plug type, and concrete plate type. In [17], wind tunnel experiment and numerical simulation computation were used to research aerodynamic performance of ventilated wind-shielding walls on bridges. In fact, wind areas on the railway line are located in the Gobi Desert area, wherein ground sand is often rolled up by strong winds and crushed vehicle glass. Hence, 3.0 m was set as the height of wind-shielding walls on railway line [18]. It is set right above the window glass of a passenger train. Meanwhile, winds on the Lanzhou-Xinjiang railway line are mainly monsoons with stable wind directions. Hence, single-side wind-shielding walls have been built on the line. In fact, due to the vast territory of China, weather conditions are quite different. For example, there are 115–160 strong-wind days along the Qinghai-Tibet line each year, while the maximum wind speed reaches 20–28 m/s [19], and the historically extreme maximum wind speed reached over 31 m/s. In Anduo district, it could reach 38 m/s [20]. In order to prevent occurrence of accidents caused by strong winds, a lot of countries have built wind-shielding walls in strong-wind areas [21–23]. However, foreign lines mainly aim at passenger trains rather than cargo trains. In China, hybrid lines are mainly built for passenger and cargo trains, while the critical overturning wind speeds of boxcars are low. Hence, in areas with high wind speeds and less sand harm, wind-shielding walls can be designed aiming at boxcars. Meanwhile, most existing wind-shielding walls of high-speed railway bridges have a nonhole structure. In comparison with the porous structure with ventilation rate of 30%, it suffers higher cross force and overturning moment in each linear meter under wind environments. If it can be applied to some long-distance overpasses (especially the second passenger transport line of the Lanzhou-Xinjiang railway line), the overall bearing loads of bridges would be reduced inevitably, which can then reduce structural stability of these bridges.

In the reported papers, the researches focus on the aerodynamic performance of the high-speed train with air barriers running on the flat ground. However, the high-speed train running on the embankment is not researched widely. Therefore, this paper conducts a numerical simulation for the unsteady flow of a high-speed train passing the embankment. Particularly, the mobile mesh technology was used to simulate the motion between a train and embankment. Unsteady pulsating pressure, unsteady flow characteristics, aerodynamic force, and aerodynamic moment characteristics embodied when the high-speed train passed the embankment air barrier were researched in details. This paper provides some engineering references for the structural optimization design, rational layout of air barriers, computing aerodynamic load intensity, and so forth concerning the high-speed train passing the air barrier.

## 2. Mathematical Model for High-Speed Train Passing the Embankment Air Barrier

As for unsteady aerodynamic flow behavior characteristics of flow fields around a high-speed train, the unsteady Reynolds time-average method stands out for its low requirement for calculated amount, but it can hardly simulate greatly separated flows such as tail flows of a high-speed train in an accurate manner [24]. The LES (large eddy simulation) method can effectively reveal large-scale eddy structures in flow fields around a train [24, 25] and can help obtain detailed transient flow-field information. But it requires very small mesh size especially near the wall face and needs a high-level computer [26]. The DES (detached eddy simulation) method combines advantages of URANS (unsteady Reynolds-averaged Navier-Stokes) and LES. Specifically, through simulation of built-in switch functions, the URANS

is applied near wall faces; the Reynolds-averaged turbulence simulation is used to process pulsation of small-scale eddies near wall faces; they are converted to a subgrid model far from the wall faces; LES is used to simulate motion of large-scale eddies [27–30]. DES combines advantages of URANS and LES, so it has been applied to simulation of unsteady flow fields around trains in recent years. Computation results are basically consistent with experimental results [31, 32].

At present, DES methods are mainly divided into two types, namely, the DES method based on SA (Spalart-Allmaras) turbulence model and the DES method based on SST (shear stress transport) two-equation model. The DES method based on SST is applied most widely in engineering [33, 34]. Hence, the paper also uses the DES method based on SST to compute flow fields of high-speed trains. Relevant formulas are as follows:

$$\frac{\partial(\rho k)}{\partial t} + \frac{\partial(\rho u_j k)}{\partial x_j} = P_k + \frac{\partial}{\partial x_j}\left[\left(\mu_t + \frac{\mu_t}{\sigma_k}\right)\frac{\partial k}{\partial x_j}\right] - \frac{\rho k^{1.5}}{l_{k-\omega}}, \tag{1}$$

$$\frac{\partial(\rho\omega)}{\partial t} + \frac{\partial(\rho u_j \omega)}{\partial u_j} = \frac{2\rho(1-F)\sigma_{\omega 2}}{\omega}\frac{\partial k}{\partial x_j}\frac{\partial \omega}{\partial x_j} + \frac{\partial}{\partial x_j}\left[\left(\mu_l + \frac{\mu_t}{\sigma_\omega}\right)\frac{\partial \omega}{\partial x_j}\right]\gamma\frac{\omega}{k}\bullet P_k - \rho\beta_1\omega^2. \tag{2}$$

In formula (1) and formula (2), $t$ is the running time of a high-speed train; $\rho$ is the density of air; $k$ is the turbulence energy of a fluid; $x_j$ is the computational coordinates; $j = 1, 2, 3$, represents the length, width, and height of coordinates, respectively; $u_j$ is a velocity component of air flow; $P_k$ is a turbulence generation item; $\sigma_\omega$, $\sigma_{\omega 2}$, $\sigma_k$, $\beta$, $\gamma$ are empirical constants and shall be determined according to design experience; $\omega$ is the specific dissipation ratio of turbulent flow of the high-speed train; $l_{k-\omega}$ is a scale parameter of the turbulent flow; $F_1$ is the switch function, representing the minimum distance between the high-speed train eddy and the wall face of computation domain. In the near-wall area of the computational domain, $F_1$ approaches 1 and the computational model approaches a $k$-$\omega$ model, so the $k$-$\omega$ model can be used to compute flow fields of the high-speed train; on boundary layer edges of the computation domain, $F_1$ approaches 0 and the computation model will be converted to a $k$-$\omega$ model. As a result, at this moment, the $k$-$\omega$ model can be used to compute flow fields of the high-speed train; $\mu_l$ denotes a laminar flow viscosity coefficient in the flow fields, and $\mu_t$ denotes a viscosity coefficient of eddies in the flow fields.

In the concerned DES method, $l_{k-\omega}$ will be replaced by $\min(l_{k-\omega}, C_{\mathrm{DES}}\Delta)$, wherein $\Delta = \max(\Delta x, \Delta y, \Delta z)$ denotes the longest edge length of mesh units in the computation domain, $C_{\mathrm{DES}} = (1 - F_1)C_{\mathrm{DES}}^{k-\varepsilon} + F_1 C_{\mathrm{DES}}^{k-\omega}$; the constant items are $C_{\mathrm{DES}}^{k-\varepsilon} = 0.61$ and $C_{\mathrm{DES}}^{k-\omega} = 0.78$; they are determined by the experience, also referred from other reported papers. In this way, $\omega$ values are quite large on boundary layers near the computation domain, and the turbulence energy $k$ values are limited in the flow fields, so $l_{k-\omega}$ will be far less than the mesh size of the computation domain, the SST turbulence model plays a dominant role, and the Reynolds time-average method is applied at this moment. $\omega$ values are very small at positions far from the high-speed train surface. When $l_{k-\omega}$ increases to a value larger than $C_{\mathrm{DES}}\Delta$, the changed model can be used as the subgrid Reynolds stress model of large eddy simulation.

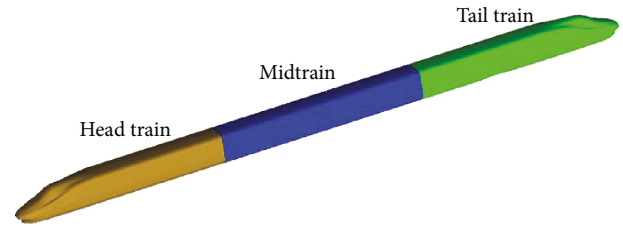


Figure 1: Simplified geometric model of the adopted high-speed train.

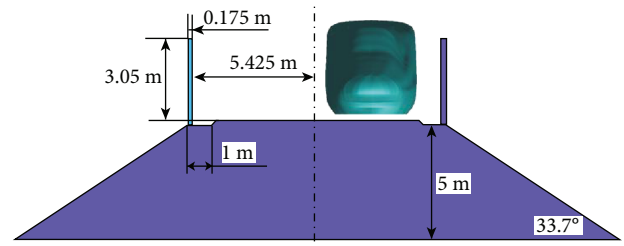


Figure 2: Geometric cross section of a high-speed train passing the embankment air barriers.

## 3. Numerical Model for High-Speed Train Passing the Embankment Air Barrier

*3.1. Geometric Model and Computational Domain.* As we know very well, the length of a high-speed train is much larger than its width and height, so it has a long and thin structure. High-speed train combination is often composed over 8 coaches. If numerical simulation is conducted to the whole train, there will be a lot of computational domains and computational meshes, leading to huge computation quantity and long computation time. The high-speed train combination only has a head and a tail, wherein a midtrain has certain distances from both ends. Flow fields are relatively stable on the middle train parts. Hence, during modeling, it is unnecessary to consider all the midtrains in the high-speed train combination. Finally, the paper adopts a model consisting of a head, a midtrain, and a tail, as shown in Figure 1. Meanwhile, to reduce the computational meshes, the train is considered as a smooth surface. Some accessories have been deleted as they will greatly increase the mesh quantity of the computational domain, increase computational time, and reduce the efficiency.

The diagram of embankment cross section is shown in Figure 2, where embankment parameters are as follows:

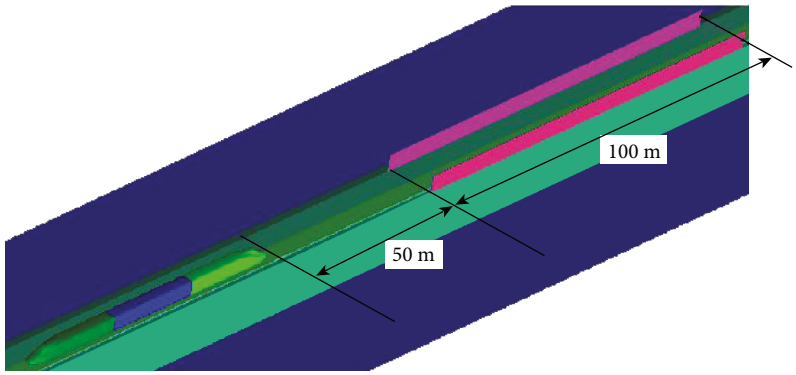


Figure 3: Geometric positions for a high-speed train passing the embankment air barriers.

upper width of 11.2 m, height of 5 m, and slope angle of 33.7°. The linear spacing of trains on the embankment is 5 m. The air barrier is 5.425 m away from the rail center line. It is 3.05 m higher than the rail face, 0.175 m thick, and 100 m long. In the paper, the air barrier close to the train body is called "air barrier close to one side of the train unit," and the air barrier far from the train body is called "air barrier far from one side of the train unit."

When a meeting train computation domain is established, sufficient development of computational flow fields and flow-passing influences of airflows are taken into account, so sizes of the computational domain must be large enough. However, the large computation domain will generate too many meshes to reduce the efficiency. In order to ensure computational reliability while increasing computation speed, many different computation models were solved. Finally, proper computation domains were selected, as shown in Figures 3 and 4. Three-dimensional sizes of flow-field computation domain are 600 m, 80 m, and 60 m, respectively. The distance between the high-speed train and rail ground is 0.3 m. The distance between the high-speed train and the air barrier is 50 m which has been validated by a lot of papers.

*3.2. Mobile Mesh Technology.* In the paper, commercial software FLUENT was used to compute aerodynamic characteristics of the high-speed train passing the embankment as the software integrates a lot of computation models. Meanwhile, FLUENT also integrates the mobile grid technology which solves the problem about relative object motion. The mobile grid technology can effectively simulate a high-speed train passing the embankment. A computation domain is divided into two regions: a mobile region and a fixed region. The mobile region represents motion of the high-speed train, while the fixed region represents the embankment. The whole computation domain of the high-speed train passing the embankment is complete. Hence, a slippage interface is used to connect the mobile and fixed regions. Flow fields of these two regions can exchange mutual information by the slippage interface. This technology is realized through addition and deletion of the whole layer of meshes as well as mobile mesh updating of nodes in the computation domain, as shown in Figure 5.

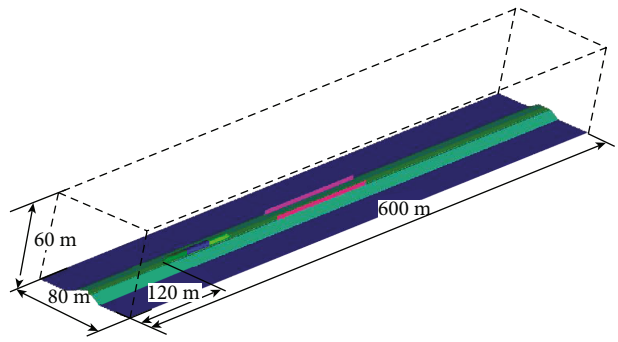


Figure 4: Computation domains of a high-speed train passing the embankment air barriers.

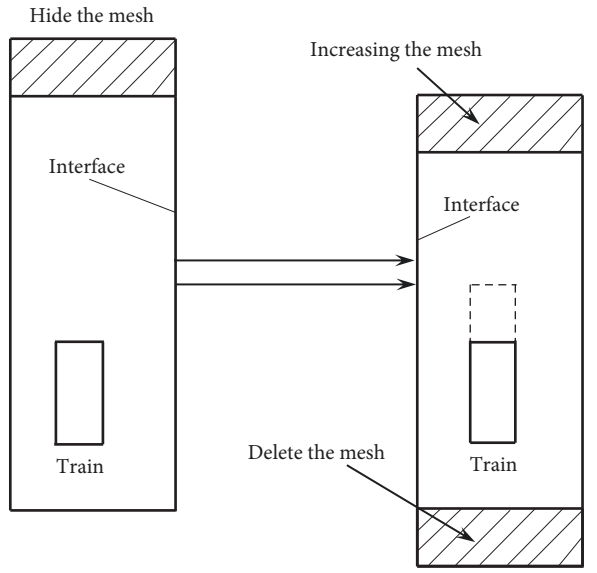


Figure 5: Diagram of the mobile mesh technology.

*3.3. Setting of Boundary Conditions.* When the high-speed train passes the embankment air barrier, the train is slipping relative to the embankment. Hence, in order to achieve the motion, the computation flow field is set to 2 neighboring regions, as shown in Figure 6. Numerical simulation of flow

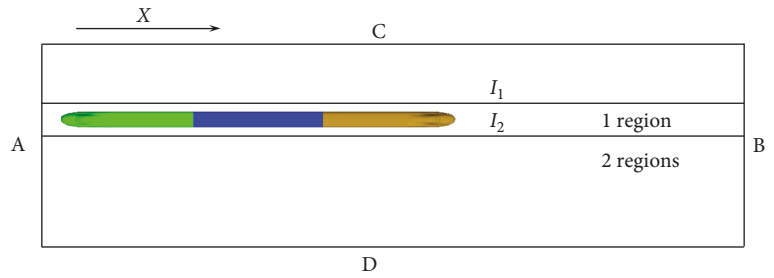


Figure 6: Two different regions for high-speed train passing the embankment air barrier.

Table 1: Verification of mesh independence.

| Mesh proposal | Outfield maximum mesh (mm) | Maximum mesh on the train surface (mm) | Total number of meshes (×10,000) | Mesh increment | Pressure at a monitoring point (Pa) | Relative variation value |
|---|---|---|---|---|---|---|
| Proposal 1 | 2500 | 100 | 2542 | | 1048 | |
| Proposal 2 | 2000 | 80 | 2890 | 13.69% | 1089 | 3.91% |
| Proposal 3 | 1500 | 70 | 3200 | 10.73% | 1110 | 1.93% |

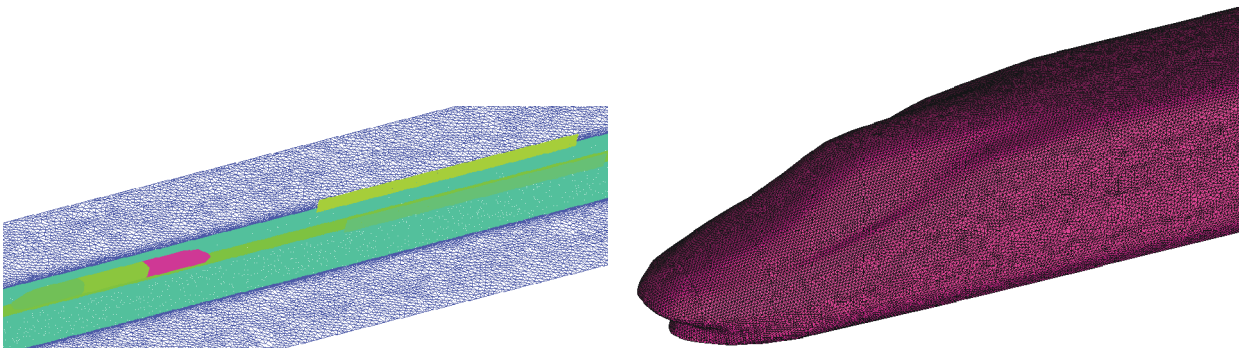

(a) Meshes in the embankment region

(b) Meshes on the head train surface

Figure 7: Mesh diagram of the high-speed train running on the embankment.

fields outside the high-speed train is completed in the finite region. Confirmed boundary conditions shall meet the self-posedness in mathematics and have a clear meaning in physics. In the computation flow field of this paper, faces A and B at the end are set as pressures, 1 standard atmospheric pressure is set, and the initial temperature is 300 K (26.85°C), and surfaces of train bodies are nonslippage wall faces.

*3.4. Discrete Mesh.* The mesh partitioning tool ICEM CFD is used to partition meshes. Meshes are unstructured tetrahedral meshes. Independence analysis is conducted to meshes. In general, when the computation error between two sets of meshes is lower than 2%, the computation results will be deemed to be irrelevant with mesh quality. In order to conduct accurate partitioning of the computation domain of high-speed trains, the paper employed three sets of meshes with different sizes for computation. Results are shown in Table 1. The total numbers of computation domains of these three models are 25.42 million, 28.9 million, and 32 million. The amount of meshes will directly determine the computational time. In other words, 32 million meshes will have the longest time. When the mesh quantity in the computation domain is 32 million, the computational error is 1.93%, lower than 2%. Hence, during the numerical computation in the paper, the number of model meshes was controlled over 32 million. In other words, the outfield maximum mesh size of the train is 1500 mm, and the maximum mesh size on the train surface is 70 mm, which can satisfy independence test requirements for meshes. Tetrahedral meshes were used for mesh partitioning of computation domains of the high-speed train. Partial spatial meshes of the high-speed train are shown in Figure 7.

## 4. Flow-Field Characteristics of the High-Speed Train Passing the Embankment Air Barrier

Figure 8 shows the surface pressure contour at the time moment of 1.125 s when the high-speed train passed the embankment air barrier at the speed of 400 km/h. It is shown in Figure 8 that the maximum pressure of the whole train is

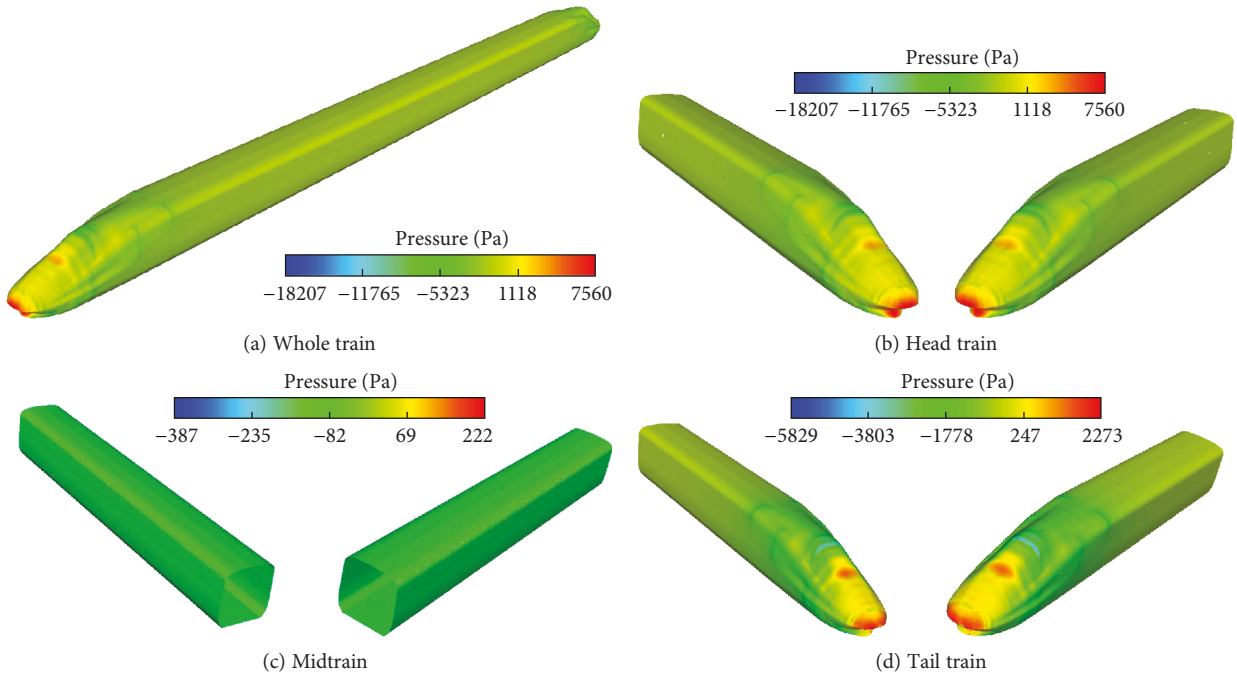


Figure 8: Pressure distribution on the train surface at 1.125 s when the high-speed train passed the air barrier.

distributed at the nose tip of the head train, with the value of 7560 Pa; the maximum negative pressure of the whole train is distributed at the pilot of the head train, with the value of 18,207 Pa. The maximum positive pressure of the tail train is distributed at the nose tip of the head train, with the value of 2273 Pa; the maximum negative pressure is distributed at the streamline transition part of the tail train, with the value of 5829 Pa. The surface pressure on the midtrain did not vary obviously, wherein the maximum pressure is 222 Pa and the maximum negative pressure is 387 Pa. Meanwhile, it is found that the shortened train model has smaller influences on computation results during aerodynamic effect computation of the embankment air barrier. These results further verify rationality of the shortened model in the paper. Additionally, the pressure distribution on the head train and tail train is very similar, and the reason is as follows. The head train will bear the incoming flow, so the nose tip of the head train will have a big pressure. In the tail region of the high-speed train, there are a lot of vortexes, so the pressure disturbance will be very obvious to cause a big pressure. However, the pressure value of the head train is obviously more than that of the tail train.

Figure 9 shows the contour of pressures distributed on the air barrier surface at 1.125 s when the high-speed train passed the embankment air barrier at the speed of 400 km/h. Through analyzing pressure distributions on the air barrier surface at the moment when the high-speed train passed the air barrier, as shown in Figure 9, we can find that the pulsation pressure of air barrier close to one side of the high-speed train (maximum positive pressure of 1390 Pa and maximum negative pressure of 1694 Pa) is more violent than the pressure pulsation of the air far from the high-speed train (maximum positive pressure of 247 Pa and maximum negative pressure of 320 Pa). When the head train passed, positive pressures were generated on front sides of both embankment air barriers. When the tail train passed, negative pressure areas were formed on rear sides of both embankment air barriers. When the head train passed the embankment air barriers, air on the front side of the head train was extruded, and static air on the front end of the train was compressed violently as air flow was blocked by the limit of embankment air barriers, so that positive pressure areas were formed on front sides of the head train and embankment air barriers, and negative pressure areas were formed on rear sides of the tail train and embankment air barriers. Pressure amplitudes on the bottom of the embankment air barrier are more than those on the top. The bottom of the embankment air barrier has better sealing performance than the top, so airflows tended to flow out from the embankment air barrier, and effective circulation areas of air on the embankment air barrier bottom are smaller than those on the bottom of embankment air barriers. Meanwhile, as for the same embankment air barrier, pulsation pressures on the side of the embankment air barrier close to the inner side of the high-speed train were larger than those on the side of the outer embankment air barrier outside the high-speed train. Results are shown in Figure 9(c).

## 5. Aerodynamic Effect of High-Speed Train Passing the Embankment Air Barrier

*5.1. Arrangement of Monitoring Points for Pulsation Pressure.* In order to figure out pressure wave relations on the train surface when the high-speed train passed embankment air barriers, pressure monitoring points were set at the same positions of the head train, midtrain, and tail train of the computed train model, as shown in Figure 10, where they

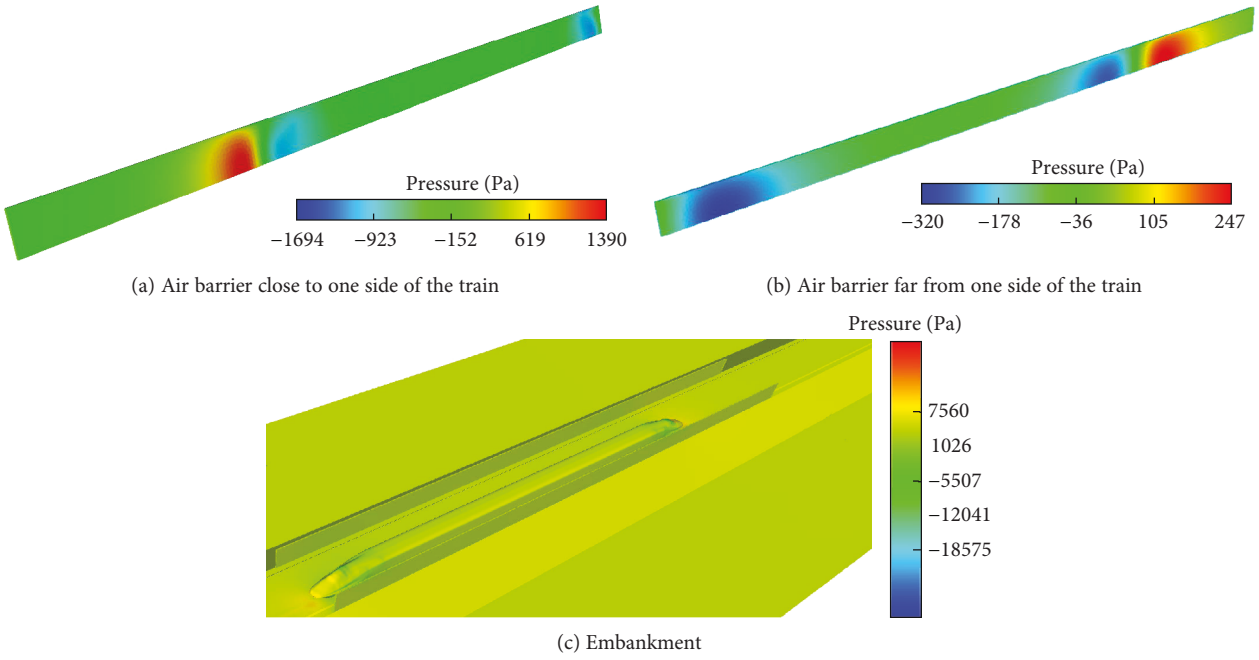


(a) Air barrier close to one side of the train

(b) Air barrier far from one side of the train

(c) Embankment

Figure 9: Contour of pressure distribution on the air barrier surface at 1.125 s.

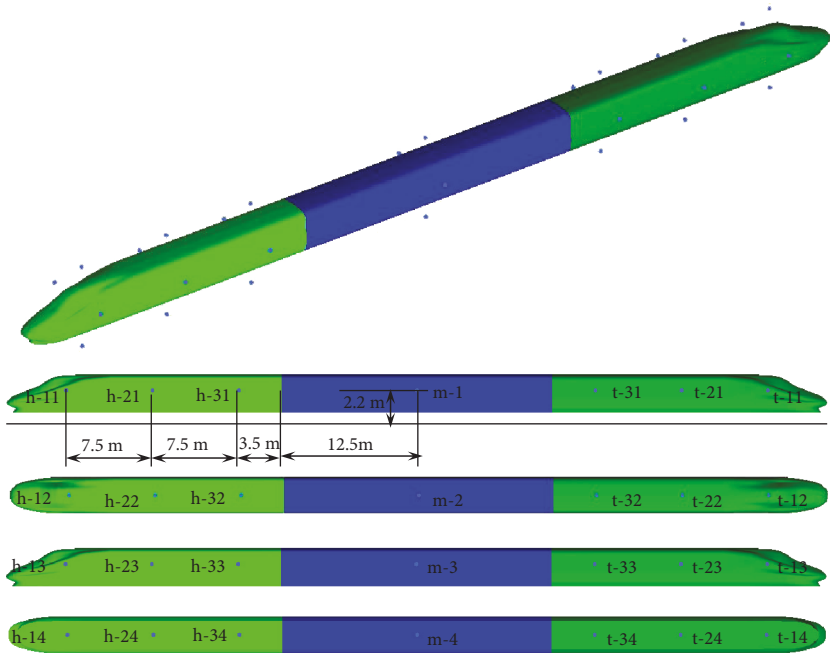


Figure 10: Layout of pressure measurement points on the train surface.

are 2.2 m higher than the ground. Therein, monitoring points h-11, h-21, h-31, m-1, t-31, t-21, and t-11 are near-wall body surface monitoring points (side nearest to the embankment air barrier); monitoring points h-12, h-22, h-32, m-2, t-32, t-22, and t-12 are monitoring points on the middle surface of the train top; monitoring points h-13, h-23, h-33, m-3, t-33, t-23, and t-13 are surface monitoring points far from the wall face (side farthest from the embankment air barrier); monitoring points h-14, h-24, h-34, m-4, t-34, t-24, and t-14 are surface pressure monitoring points at middle parts of high-speed train bottom. Specific pressure monitoring point positions on the train surface are shown in Figure 10.

*5.2. Characteristics of Pulsation Pressure.* Figure 11 shows curves of pressure changing at the side window (pressure monitoring point h-11) which is located close to the

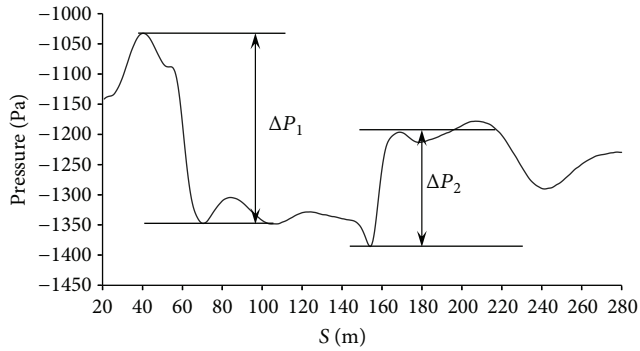


Figure 11: Curve of pressure changes at monitoring point h-11 under the train passing the air barrier.

embankment air barrier when the high-speed train passed the embankment air barrier at the speed of 350 km/h. The following are shown in Figure 11:

(1) The amount used to describe the air pressure fluctuation size of the train passing the embankment air barrier is the air pressure wave amplitude, which is also marked as full wave and represented by $\Delta P$, as below:

$$\Delta P = \begin{cases} |\Delta P_+| + |\Delta P_-|, & |\Delta P_+| + |\Delta P_-| \le 0, \\ ||\Delta P_+| - |\Delta P_-||, & |\Delta P_+| + |\Delta P_-| > 0. \end{cases} \tag{3}$$

(2) During the period before the train head reached the side window monitoring point of the embankment air barrier, the pressure had already started increasing and then increased quickly. When the train nose tip reached the measurement point, a positive-negative pulsation was generated, namely, the head wave; constant-amplitude fluctuation started when the maximum negative pulsation appeared, and a negative-positive pulsation was generated when the tail train nose tip passed the monitoring point, namely, the tail wave.

(3) The amount used to describe air pressure wave intensity under the train passing the air barrier is the time gradient of pressure waves, namely,

$$\text{grad}\,\nabla P = \frac{\Delta P}{\Delta t}. \tag{4}$$

(4) Pressure coefficient is defined as

$$C_p = \frac{2P}{\rho v^2}, \tag{5}$$

where $P$ is the aerodynamic pressure, $\rho$ is the used air density, and $v$ is the running speed.

*5.3. Distribution Rules of Pulsation Pressure.* In order to research distribution rules of pressure changes on the train surface, which happened when the high-speed train passed the embankment air barrier, pressure monitoring was conducted to each point. The pressure changing curves of monitoring points on different cross sections are obtained, as shown in Figure 12. Through analyzing Figure 12, we can find the following:

(1) The head wave of the air pressure full wave was more than the tail wave when the train passed the embankment air barrier; the absolute values of negative waves were larger than those of positive waves, and the phenomenon was more obvious on the head car. When the train passed the air barrier, pressure pulsations at monitoring points of the head train were larger than pulsation pressures of other monitoring points. Pressure changes at monitoring points of the train bottom were most violent.

(2) The head wave pressure peak value was 426 Pa at the monitoring point h-11 of the cross section 1, while the tail wave peak value was 333 Pa; for monitoring point h-12, the head wave pressure peak value was 329 Pa, and the tail wave peak value was 176 Pa; for the monitoring point h-13, the head wave pressure wave peak value was 319 Pa, and the tail wave peak value was 187 Pa; for the monitoring point h-14, the head wave pressure peak value was 562 Pa, and the tail wave peak value was 499 Pa.

(3) At the monitoring point h-21 of cross section 2, the head wave pressure peak value was 395 Pa, and the tail wave peak value was 114 Pa; at the monitoring point h-22, the head wave pressure peak value was 258 Pa, and the tail wave peak value was 168 Pa; for the monitoring point h-23, the head wave pressure peak value was 281 Pa, and the tail wave peak value was 110 Pa; for the monitoring point h-24, the head wave pressure peak value was 383 Pa, and the tail wave peak value was 211 Pa. Pressure peak values of other monitoring points did not have obvious differences. Hence, specific values of them are not listed in the paper.

(4) According to pressure curves of monitoring points on different cross sections, we can find that when the high-speed train passed the embankment air barrier, pressure pulsations changed violently at different monitoring points, and the pressures were negative; pressure values at monitoring points close to the air barrier were larger than those of the monitoring point far from the air barrier. Pressure values of monitoring points at cross section 1 were larger than those of other monitoring points. The maximum negative pressure amplitude reached 1549 Pa; the pressure peak value reached 562 Pa; maximum pressure changes were 452 Pa/3 s and 159 Pa/1 s. Pressure values at monitoring points of the tail train ranked the second place. The maximum negative pressure value was 1253 Pa.

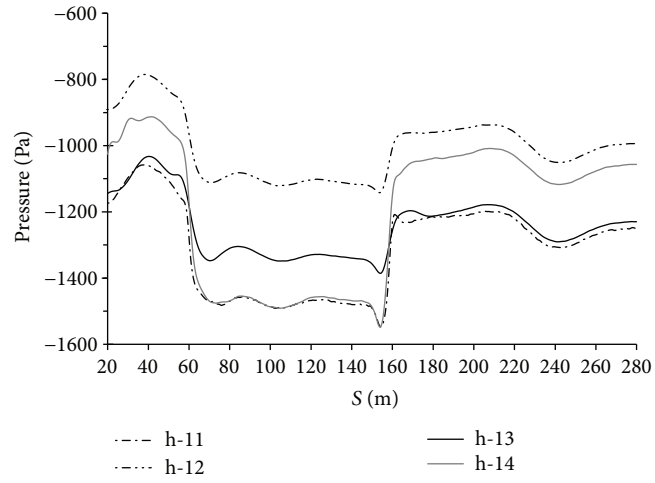


(a) Monitoring points h-1

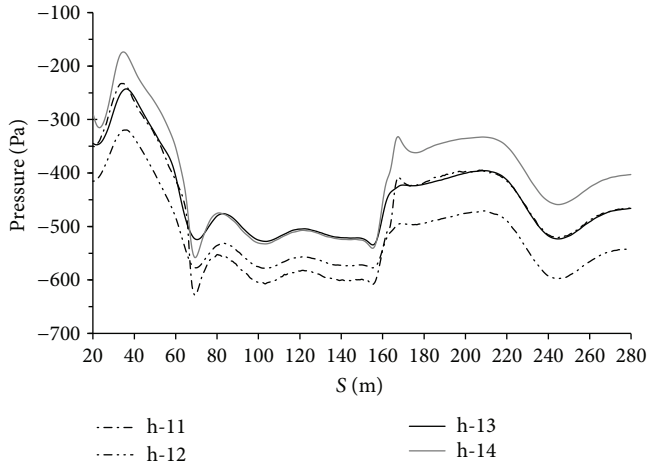


(b) Monitoring points h-2

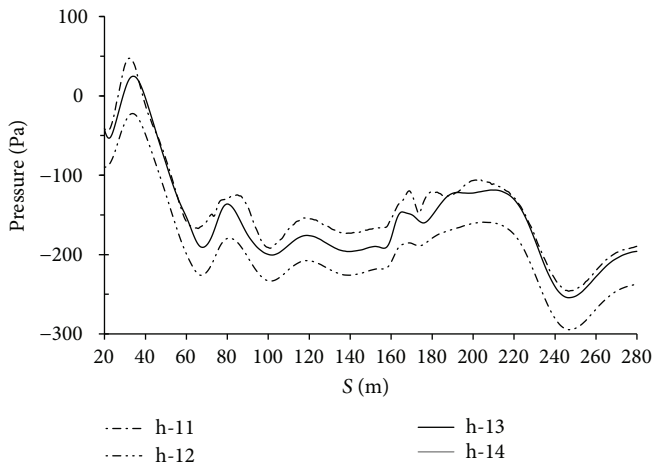


(c) Monitoring points h-3

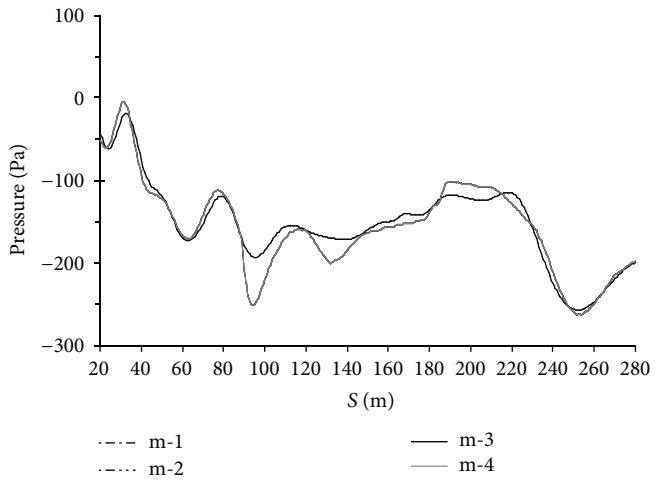


(d) Monitoring points of mid train

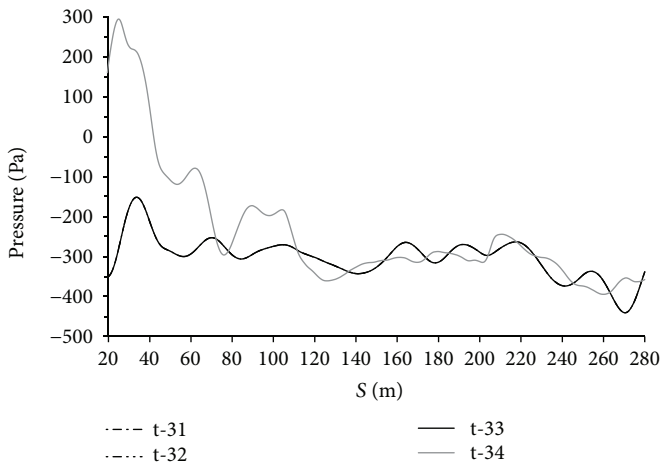


(e) Monitoring points t-3

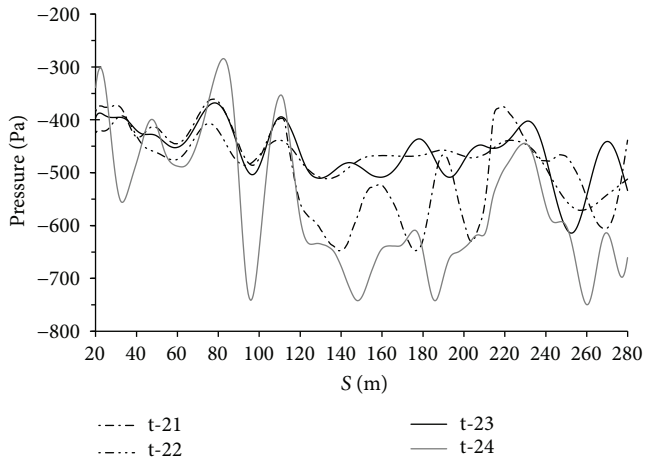


(f) Monitoring points t-2

Figure 12: Continued.

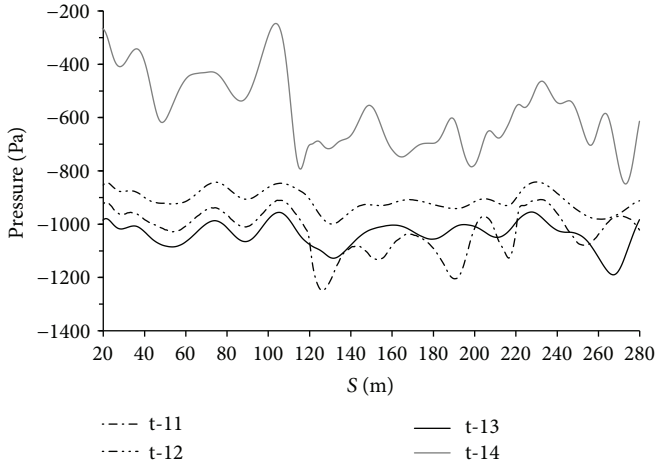


(g) Monitoring points t-1

Figure 12: Pressure change curves at different monitoring points.

(5) Along the train running direction, pressure fluctuation distribution rules became less obvious. Pressure pulsation distribution of the midtrain and tail train showed no rules, and pressure fluctuation was small. Pulsation pressure distribution rules of the head train satisfy pressure pulsation distribution rules under the train meeting case: the pressure peak value of the head wave was larger than the pressure peak value of the tail train; pressure pulsations at the train bottom were larger than those of other monitoring points; the pressure pulsation was most obvious at the monitoring point h-14.

*5.4. Speed-Based Changing Rules of Pulsation Pressure.* Figure 13 shows comparative curves of pressure changes on the train surface close to the air barrier, which took place when the high-speed train passed the embankment air barrier at different running speeds of 400 km/h, 500 km/h, and 600 km/h. Through curve comparison in Figure 13, it is found that influences of the embankment air barrier structure on pressure monitoring points of the head train were larger than influences on the tail train. The head wave pressure peak value and tail wave pressure peak value of the head train were larger than those of the tail train. Additionally, the pressure was increased with the increase of the running speed of the high-speed train because the interaction between the high-speed train and fluids will be more serious. The interaction will cause aerodynamic pressures.

When the high-speed train passed the embankment air barrier at speeds of 400 km/h, 500 km/h, and 600 km/h, the head wave pressure peak values at monitoring points h-11 were 204 Pa, 318 Pa, and 429 Pa, respectively. Through curve fitting, the relation (6) could be obtained and pressure time-interval curves of different monitoring points could be obtained. It is found that aerodynamic influences existing when the head train passed were larger than those taking place when the tail train passed.

$$\Delta P = 0.0154v^2, \tag{6}$$

where $\Delta P$ denotes the head wave pressure peak value of the head train and $v$ denotes the running speed of the high-speed train which passed the embankment air barrier. In the paper, running speeds of 400 km/h (111.1111 m/s), 500 km/h (138.8889 m/s), and 600 km/h (166.6667 m/s) were set for the train.

When the high-speed train passed the embankment air barrier at speeds of 400 km/h, 500 km/h, and 600 km/h, the head wave pressure peak values of monitoring point h-14 were 239 Pa, 395 Pa, and 562 Pa. Through curve fitting, the relation (7) between pressure peak values and train running speeds was obtained. Obviously, the head wave pressure peak values were in direct ratio to squares of train running speeds.

$$\Delta P = 0.0201v^2. \tag{7}$$

*5.5. Aerodynamic Load Characteristics under High-Speed Train Passing the Embankment Air Barrier.* Computation coordinates of aerodynamic forces under the high-speed trains passing the embankment air barrier are shown in Figure 14. In fact, the computational coordinates can be selected in other positions of the high-speed train. In this paper, in order to compute the aerodynamic conveniently, we have selected the computational coordinates in the mid-train of the high-speed train. $F_x$ denotes the drag force, $F_y$ denotes the side force, $F_z$ denotes the lift force, $M_x$ denotes the shaking moment, $M_y$ denotes the nod moment, and $M_z$ denotes the overturning moment. Aerodynamic force is extracted through area integration of the outer train surface. In the paper, the simplified center of aerodynamic moments is shown in Figure 14. The moment center is 2.2 m higher than the ground.

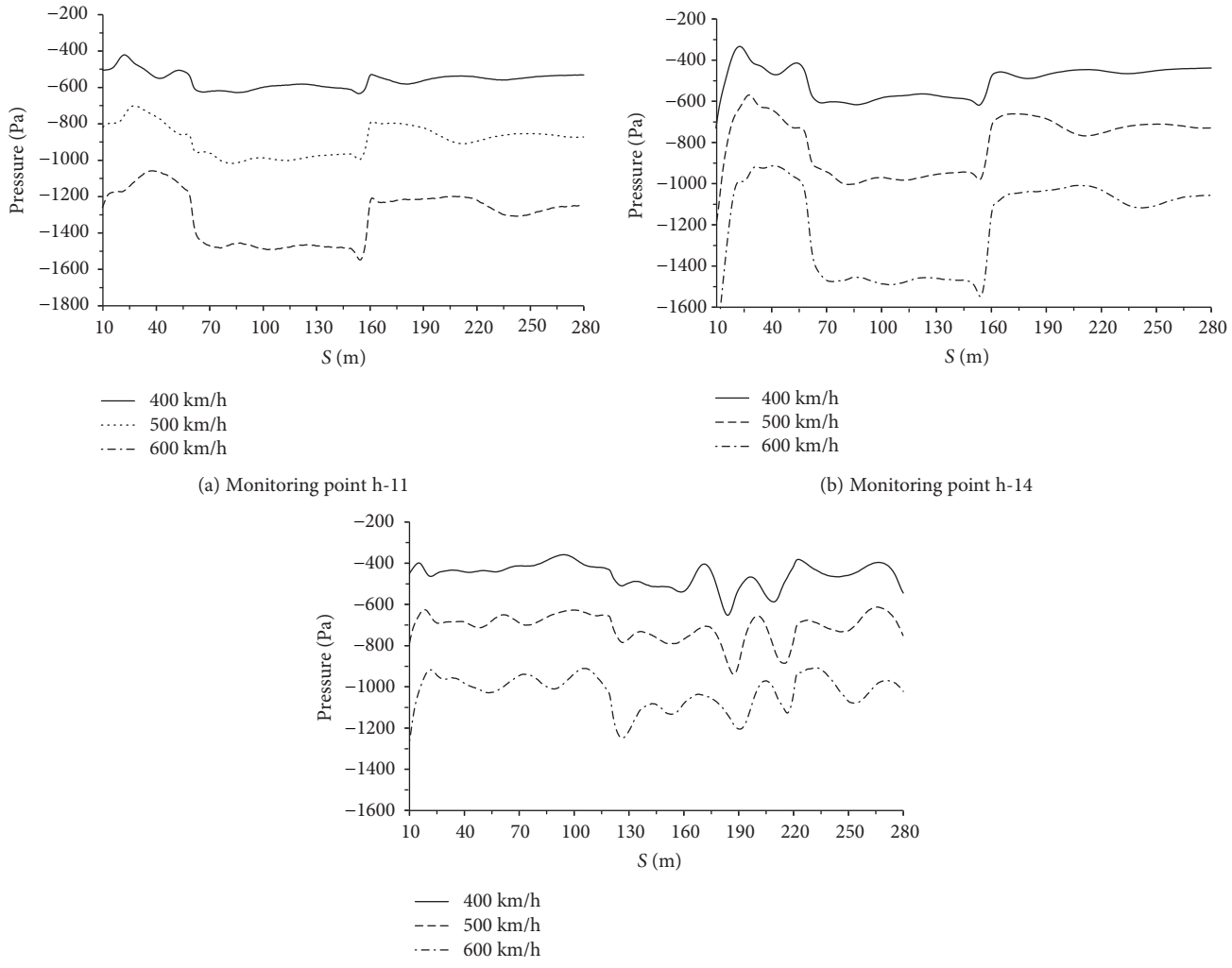


Figure 13: Comparison curves of pressures at different monitoring points under high-speed train passing the embankment air barrier.

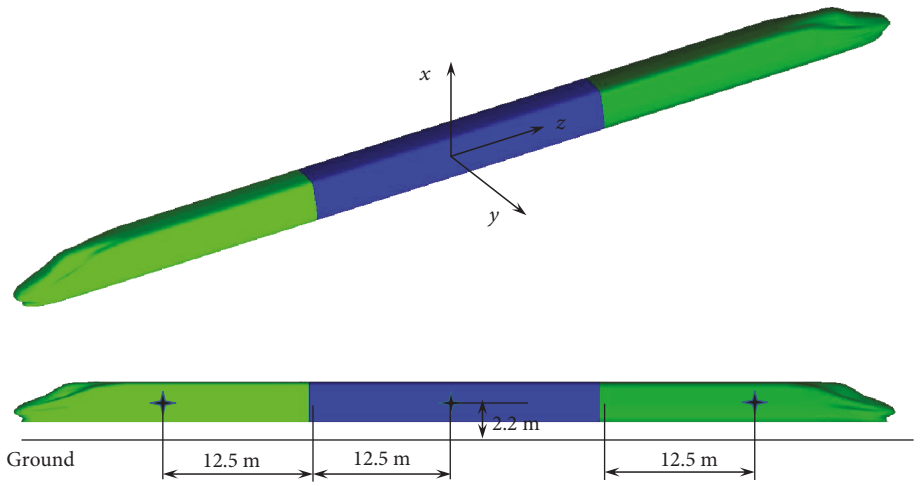


Figure 14: Diagram of aerodynamic moment positions.

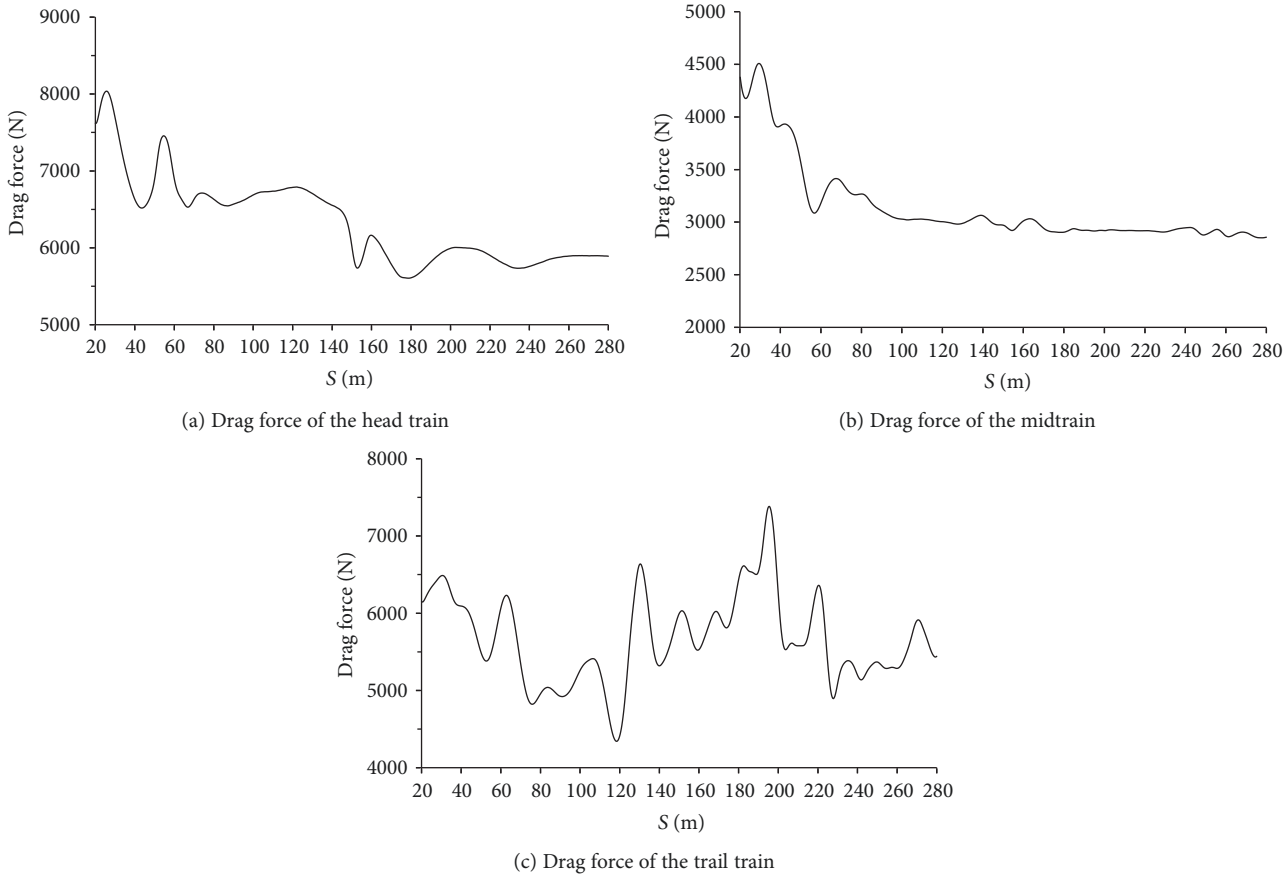


(a) Drag force of the head train

(b) Drag force of the midtrain

(c) Drag force of the trail train

Figure 15: Changing of aerodynamic drag force of each train body.

Figure 15 shows time-based changing curves of drag force borne by the high-speed train when it passed the embankment barrier at 400 km/h. The following are found through comparison of drag force changing curves, as shown in Figure 15:

(1) When the high-speed train left and passed the embankment air barrier, the head train suffered the largest drag force; drag force suffered by the tail train ranked the second place, and the midtrain suffered the minimum drag force. When the train passed the embankment air barrier, the unsteady characteristics of the tail train drag force were obvious, and the drag force changed violently. When the head train left the embankment air barrier, the head train drag force changed obviously, and influences were obvious. The embankment air barrier structure only exerted obvious influences on the midtrain drag force when the midtrain entered the embankment air barrier, wherein the drag force decreased quickly and after that, the fluctuation of the drag force changes became increasingly smaller.

(2) With the increase of running speed of the high-speed train, drag force changing peaks and maximum amplitudes were in direct ratio to the square of the train running speed.

Figure 16 shows comparative curves of speed-based changing of lift force on each train body, which took place when the high-speed train passed the embankment air barrier. The following are shown in Figure 16:

(1) Along the running direction of the high-speed train, lift force values of the midtrain and tail train of the high-speed train were positive and had an upward direction. The tail train of each train generated the maximum lift force influences. The lift force peak values of the head wave were larger than the lift force peak values of the tail wave. In other words, the lift force changing amplitude of the tail train under the high-speed train entering into the embankment air barrier was larger than the lift force changing amplitude of the tail train under the train leaving from the embankment air barrier. The tail wave lift force peak value of the head train was larger than the head train lift fore peak value. In other words, the lift force changing amplitude of the head train under the high-speed train entering into the embankment air barrier was smaller than the lift force changing amplitude of the head train under the train leaving from the embankment air barrier. The head wave lift force peak value of the midtrain was larger than the lift force peak value of the tail wave.

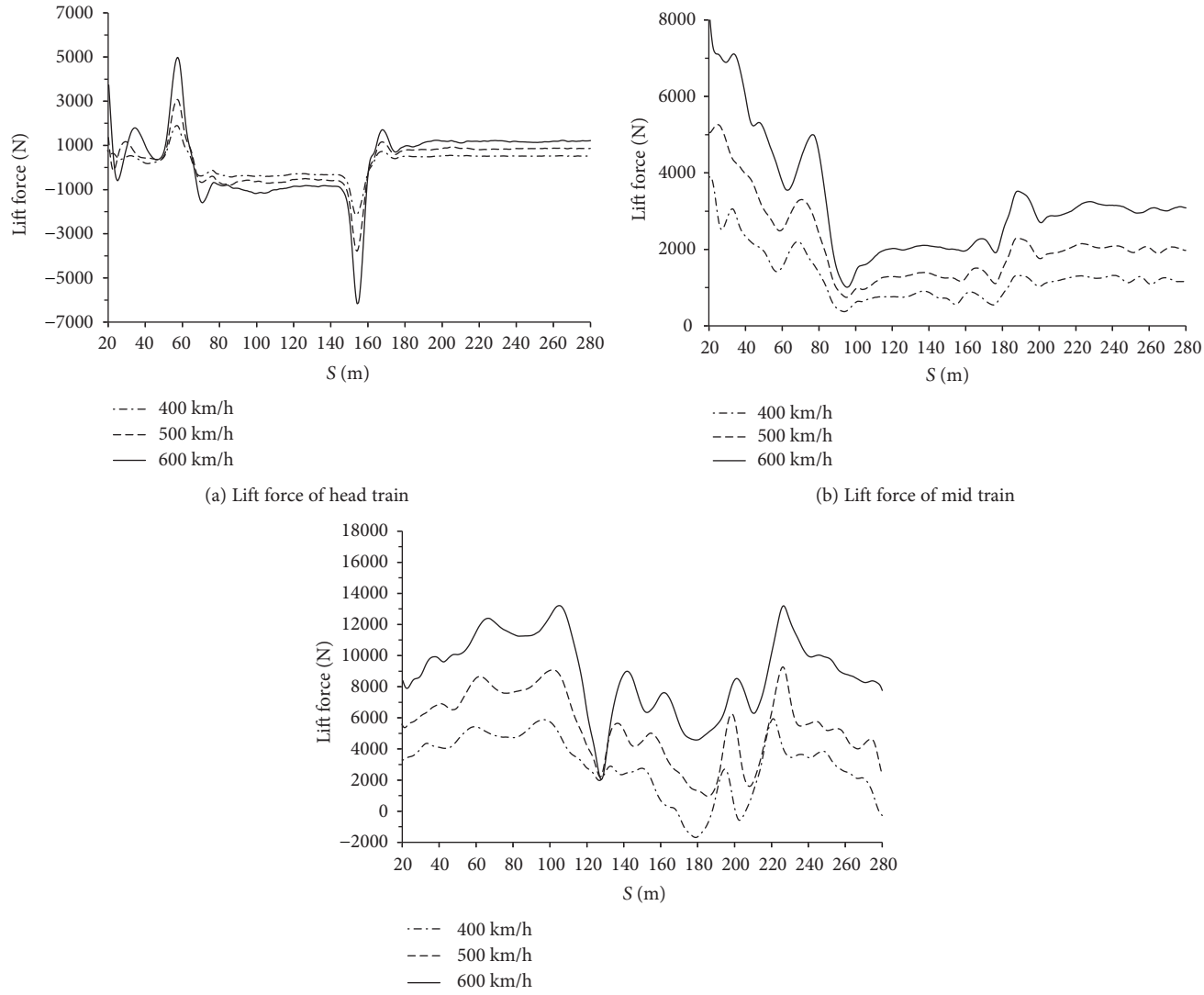


(a) Lift force of head train

(b) Lift force of mid train

(c) Lift force of tail train

Figure 16: Changing of aerodynamic lift force of each train body.

(2) When the high-speed train passed the entrance of the embankment air barrier, positive lift fore peaks were generated on head train, midtrain, and tail train of the train at first, and then the lift force sharply decreased to lift force peak-to-valley values. When the tail of the high-speed train passed the exit of the embankment air barrier, a lift force peak-to-valley value was generated at first, and then the lift force increased sharply to its positive peak value.

(3) With the increase of running speed of the high-speed train, the changing peak values and maximum amplitudes of the lift force were in direct ratio to squares of train running speeds.

Figure 17 gives comparative curves of side forces with running speeds on each train body, which took place when the high-speed train passed the embankment air barrier. The following are found through comparative analyzing Figure 17:

(1) When the high-speed train passed the entrance of the embankment air barrier, a negative side force peak was generated on the head train at first (side force direction is the direction far from the air barrier), and then the side face sharply decreased to the side force peak-to-valley value; when the head of the high-speed train passed the exit of the embankment air barrier, a side force peak-to-valley value was generated at first, and then the side force sharply increased to a positive side force peak value (side force direction is close to the side of air barrier).

(2) Side force changes of the midtrain increased with the running speed of the high-speed train, and these changes had no rules. Side force amplitudes of the tail

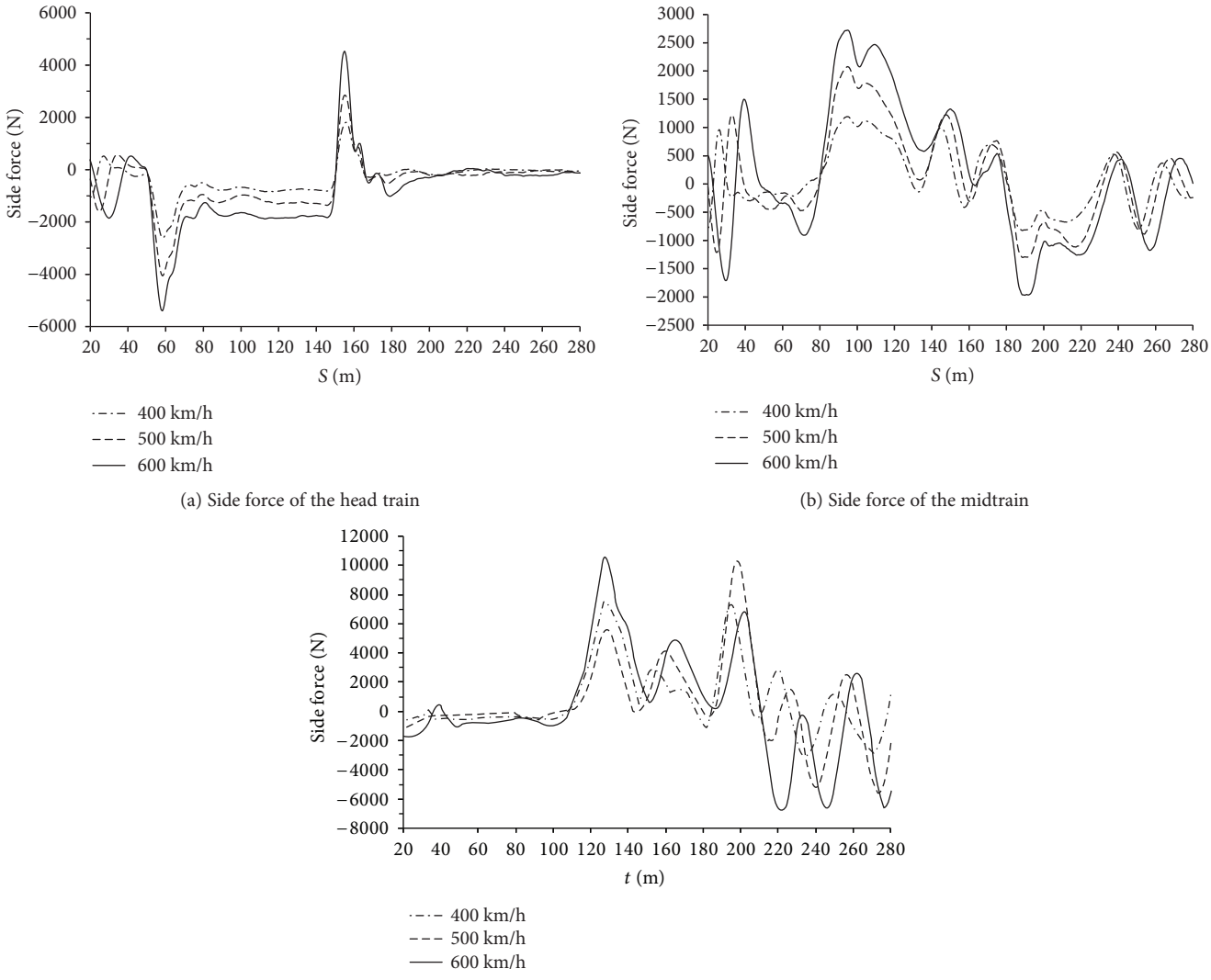


(a) Side force of the head train

(b) Side force of the midtrain

(c) Side force of the tail train

Figure 17: Changing of aerodynamic side force of each train body.

train were positive when the train passed the embankment air barrier. Obviously, the tail train inclined to the side near the air barrier in the horizontal direction.

(3) With the running speed of the high-speed train, changing peak values and maximum amplitudes of the side force were in direct ratio to squares of train running speeds.

Figure 18 shows comparative curves of aerodynamic moments on the head train, which took place when the high-speed train passed the embankment air barrier at 400 km/h. The following are found through comparatively analyzing Figure 17:

(1) When the high-speed train passed the entrance of the embankment air barrier, a positive shaking moment peak value was generated to the head train at first (in the direction remote from the embankment air barrier); when the train passed the embankment air barrier, the overturning moment directions of the head train were far from the remote side of the embankment air barrier When the head train left the exit of the embankment air barrier, the peak values decreased sharply to that under a flat ground case, namely, the shaking moment approached −6000 N·m. Changing in the shaking moment of the midtrain and shaking moment of the tail train did not show any rule. With the increase of train running speed, amplitudes increased rapidly.

(2) When the high-speed train passed the entrance of the embankment air barrier, positive nod moment peaks were generated to the head train, midtrain, and tail train at first (the direction of nod moment borne by the train was upward). When the head train, midtrain, and tail train left the exit of the embankment air barrier, the peak values decreased sharply to the

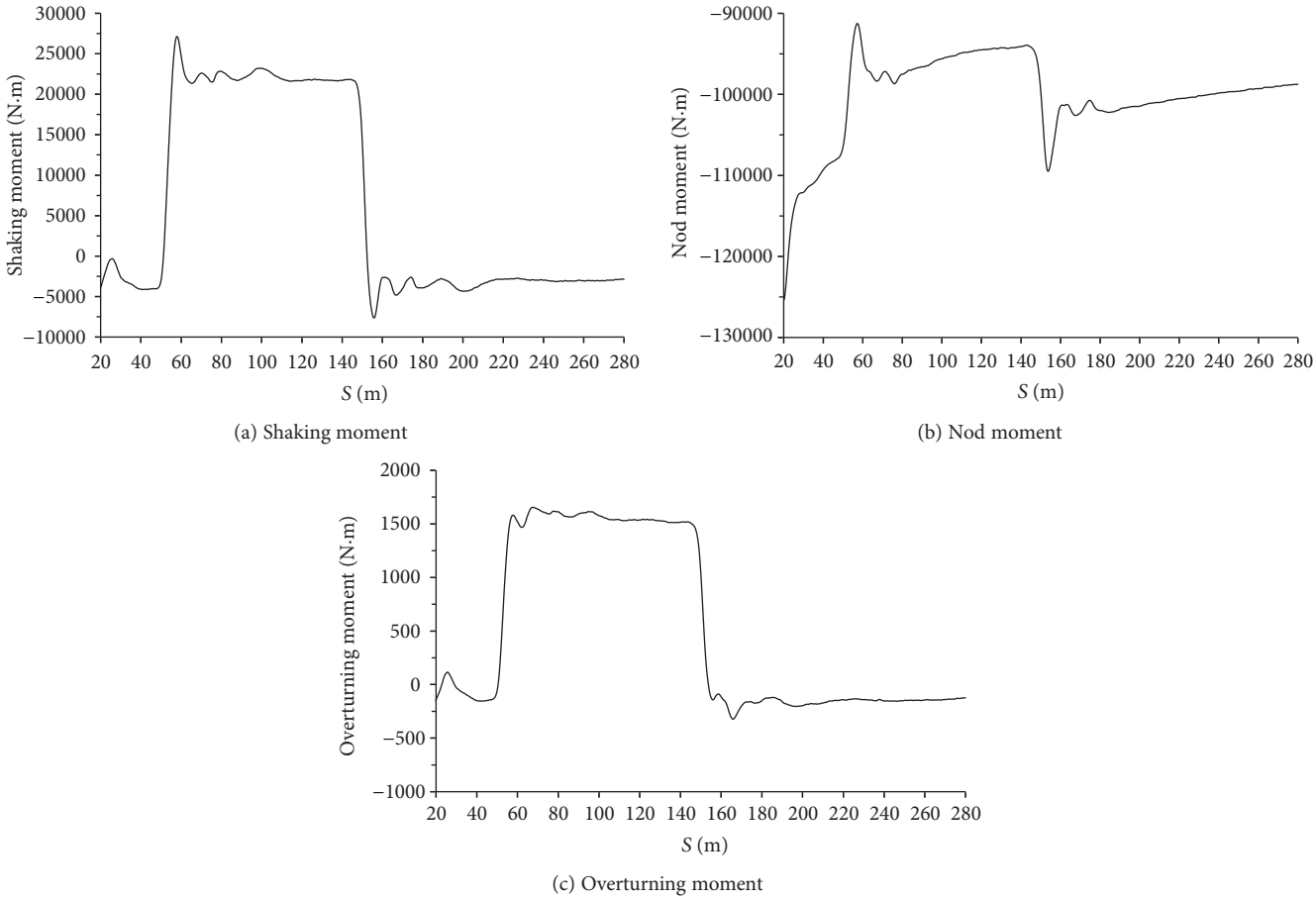


(a) Shaking moment

(b) Nod moment

(c) Overturning moment

Figure 18: Changing of aerodynamic moments of the head train.

peak-to-valley values of nod moments and then sharply increased to values under the flat ground case. All the nod moments were negative, namely, nod moments were downward when the train passed the embankment air barrier. With the increase of train running speed, the amplitudes increased rapidly.

(3) When the high-speed train passed the entrance of the embankment air barrier, a positive overturning moment peak value was generated to the head train at first (in the direction close to the air barrier); when the train passed the embankment air barrier, directions of overturning moments of the head train were close to the side near the embankment air barrier. When the head train left the exit of the embankment air barrier, the peak value decreased sharply to that under the flat ground case, namely, the overturning moment value was larger than 0. Overturning moment changes of the midtrain and tail train did not show any rule. With the increase of train running speed, amplitudes increased rapidly.

## 6. Conclusions

In the paper, numerical simulation analysis was conducted to pressure pulsations and aerodynamic acting force (moments) of a high-speed train passing the embankment air barrier through using CFD finite volume method and mobile mesh technology. The following conclusions were obtained:

(1) The maximum positive pressure of the whole train was located at the nose tip of the head train; the maximum negative pressure of the whole train was distributed at the head train pilot. Pressure changes on the surface of the midtrain were not obvious. Pulsation pressure of the air barrier near the train was more violent than the air barrier pressure pulsation remote from the train.

(2) When the train passed the embankment air barrier, the head wave was more than the tail wave; the absolute value of the negative wave was larger than that of the positive wave, while the phenomenon was more obvious on the head train. When the train passed the air barrier, pressure pulsation values at monitoring points of the head train were larger than pulsation pressure values at other monitoring points, while the most obvious pressure changes appeared at monitoring points of the train bottom. When the high-speed train passed the embankment air barrier, pressure pulsation changed obviously at each monitoring point; all the pressure values were negative; pressure

values of monitoring points near the air barrier were larger than those of monitoring points far from the air barrier. Along the train running direction, distribution rules of pressure fluctuation became less obvious. Pressure pulsation distribution of the midtrain and tail train had no rules, and pressure fluctuation was not obvious.

(3) With the increase of high-speed train running speed, when the train travelled in the embankment air barrier, changing amplitudes and maximum negative pressures on the train surface increased quickly. It could be approximately deemed that the maximum pressure peak value was in direct ratio to the square of train running speed. Under different speed levels, different train bodies satisfied $\Delta P = 0.0154v^2$ at the monitoring point h-11; at the monitoring point h-14, the head wave pressure peak value and the train running speed satisfied $\Delta P = 0.0201v^2$. Obviously, the pressure peak value was in direct ratio to the square of train running speed.

(4) With the increase of running speed of high-speed train, when the train travelled in the embankment air barrier, aerodynamic acting force (drag force, lift force, and side force) and aerodynamic moments (overturning moment, shaking moment, and nod moment) borne by each train body increased sharply. In subsequent researches, dynamic computation of the high-speed train can be taken into account for further assessment of safety and comfort during a high-speed train passing at the embankment air barrier. This paper only proposed one computational method to predict the aerodynamic performance of the mega high-speed train caused by the wind barrier on the embankment. In the future work, we will try to use this method to select and arrange the optimal air barrier.

## Data Availability

The data used to support the findings of this study are available from the corresponding author upon request.

## Conflicts of Interest

The authors declare that they have no conflicts of interest.

## Acknowledgments

This work is supported by the National Natural Science Foundation of China (Grant no. 51667017) and Key Research Projects of Tibet Autonomous Region for Innovation and Entrepreneur (Grant no. Z2016D01G01/01).

## References

[1] R. S. Raghunathan, H. D. Kim, and T. Setoguchi, "Aerodynamics of high-speed railway train," *Progress in Aerospace Sciences*, vol. 38, no. 6-7, pp. 469–514, 2002.

[2] S. Sanquer, C. Barré, M. D. de Virel, and L.-M. Cléon, "Effect of cross winds on high-speed trains: development of a new experimental methodology," *Journal of Wind Engineering and Industrial Aerodynamics*, vol. 92, no. 7-8, pp. 535–545, 2004.

[3] J. Pombo, J. Ambrósio, M. Pereira, F. Rauter, A. Collina, and A. Facchinetti, "Influence of the aerodynamic forces on the pantograph–catenary system for high-speed trains," *Vehicle System Dynamics*, vol. 47, no. 11, pp. 1327–1347, 2009.

[4] B. Li, *Wind Disaster and Its Countermeasures in Wind Region of Lanzhou-Xinjiang Railway Line*, vol. 6, Landbridge Horizon, 2007.

[5] T. Fujii, T. Maeda, H. Ishida, T. Imai, K. Tanemoto, and M. Suzuki, "Wind-induced accidents of train/vehicles and their measures in Japan," *Quarterly Report of RTRI*, vol. 40, no. 1, pp. 50–55, 1999.

[6] J. Zhang and T. H. Liu, "Optimization research on the slope angle of the earth type windbreak wall of Xinjiang single-track railway," *China Railway Science*, vol. 33, no. 2, pp. 28–32, 2012.

[7] T. Imai, T. Fujii, K. Tanemoto et al., "New train regulation method based on wind direction and velocity of natural wind against strong winds," *Journal of Wind Engineering and Industrial Aerodynamics*, vol. 90, no. 12–15, pp. 1601–1610, 2002.

[8] B. Lin, "Wind-resistant construction technology of bridge in 100km wind area of south Xinjiang," *Construction Technology*, vol. 41, no. 360, pp. 65–69, 2012.

[9] X. B. Li, Z. Yang, J. Y. Zhang, and W. H. Zhang, "Aerodynamics properties of high-speed train in strong wind," *Journal of Traffic and Transportation Engineering*, vol. 9, no. 2, pp. 66–73, 2009.

[10] T. H. Liu and J. Zhang, "Effect of landform on aerodynamic performance of high-speed trains in cutting under cross wind," *Journal of Central South University*, vol. 20, no. 3, pp. 830–836, 2013.

[11] D. Zhou, H. Q. Tian, and Z. J. Lu, "Influence of strong cross-wind on aerodynamic performance of passenger train running on embankment," *Journal of Traffic and Transportation Engineering*, vol. 7, no. 4, pp. 6–9, 2007.

[12] G. J. Gao and L. L. Duan, "Height of wind barrier on embankment of single railway line," *Journal of Central South University (Science and Technology)*, vol. 42, no. 1, pp. 254–259, 2011.

[13] Y. F. Li, H. Q. Tian, and H. Liu, "Optimization of windbreak wall with holes in high-speed railway," *Journal of Central South University (Science and Technology)*, vol. 42, no. 10, pp. 3207–3212, 2011.

[14] F. H. Liu, "Wind-proof effect of different kinds of windbreak walls on the security of trains," *Journal of Central South University (Science and Technology)*, vol. 37, no. 1, pp. 166–182, 2006.

[15] C. X. Jiang and X. F. Liang, "Effect of the vehicle aerodynamic performance caused by the height and position of wind-break wall," *China Railway Science*, vol. 27, no. 2, pp. 66–70, 2006.

[16] S. Avila-Sanchez, S. Pindado, O. Lopez-Garcia, and A. Sanz-Andres, "Wind tunnel analysis of the aerodynamic loads on rolling stock over railway embankments: the effect of shelter windbreaks," *The Scientific World Journal*, vol. 2014, Article ID 421829, 17 pages, 2014.

[17] M. A. Barcala and J. Meseguer, "An experimental study of the influence of parapets on the aerodynamic loads under cross wind on a two-dimensional model of a railway vehicle on a

bridge," *Proceedings of the Institution of Mechanical Engineers, Part F: Journal of Rail and Rapid Transit*, vol. 221, no. 4, pp. 487–494, 2007.

[18] G. Y. Zeng, "Wind barrier survey and design in wind region of Lanzhou-Xianjiang railway," *Subgrade Construction*, vol. 81, no. 6, pp. 24–29, 1998.

[19] D. C. Qiu, "The trait of the railway stations and yards design in the permafrost regions of the Qinghai-Tibet railway," *Journal of Glaciology and Geocryology*, vol. 25, no. Z1, pp. 133–135, 2003.

[20] H. Z. Bai, D. L. Li, A. X. Dong, and F. Fang, "Strong wind and wind pressure along the Qinghai-Tibet railway," *Journal of Glaciology and Geocryology*, vol. 27, no. 1, pp. 111–116, 2005.

[21] S. Avila-Sanchez, O. Lopez-Garcia, A. Cuerva, and J. Meseguer, "Characterisation of cross-flow above a railway bridge equipped with solid windbreaks," *Engineering Structures*, vol. 126, pp. 133–146, 2016.

[22] Q. K. Liu, Y. L. Du, and F. G. Qiao, "Train crosswind and strong wind countermeasure research in Japan," *Journal of the China Railway Society*, vol. 30, no. 1, pp. 82–88, 2008.

[23] Q. P. Sheng, "Side wind problem in high-speed railway," *Railway Standard Design*, vol. 4, pp. 19–21, 2006.

[24] H. Hemida, S. Krajnovic, and L. Davidson, "Large-eddy simulation of the flow around a simplified high speed train under the influence of a cross-wind," in *17th AIAA Computational Fluid Dynamics Conference,* p. 5354, Toronto, Ontario, Canada, June 2005.

[25] H. Hemida and S. Krajnovic, "LES study of the influence of a train-nose shape on the flow structures under cross-wind conditions," *Journal of Fluids Engineering*, vol. 130, no. 9, article 091101, 2008.

[26] C. Baker, "The flow around high speed trains," *Journal of Wind Engineering and Industrial Aerodynamics*, vol. 98, no. 6-7, pp. 277–298, 2010.

[27] M. Strelets, "Detached eddy simulation of massively separated flows," in *39th Aerospace Sciences Meeting and Exhibit*, Reno, NV, USA, 2001.

[28] H. Ghuge, *Detached Eddy Simulations of a Simplified Tractor-Trailer Geometry, [MS Thesis]*, Auburn University, Alabama, 2007.

[29] T. Nishino, G. T. Roberts, and X. Zhang, "Unsteady RANS and detached-eddy simulations of flow around a circular cylinder in ground effect," *Journal of Fluids and Structures*, vol. 24, no. 1, pp. 18–33, 2008.

[30] P. R. Spalart, "Detached-eddy simulation," *Annual Review of Fluid Mechanics*, vol. 41, no. 1, pp. 181–202, 2009.

[31] L. Zhang, J. Y. Zhang, T. Li, and W. H. Zhang, "Research on unsteady aerodynamic characteristics of pantographs in different positions of high-speed trains," *Journal of Mechanical Engineering*, vol. 53, no. 12, pp. 147–155, 2017.

[32] T. Favre and G. Efraimsson, "An assessment of detached-eddy simulations of unsteady crosswind aerodynamics of road vehicles," *Flow, Turbulence and Combustion*, vol. 87, no. 1, pp. 133–163, 2011.

[33] F. R. Menter and M. Kuntz, "Adaptation of eddy-viscosity turbulence models to unsteady separated flow behind vehicles," in *The Aerodynamics of Heavy Vehicles: Trucks, Buses, and Trains*, pp. 339–352, Springer Berlin Heidelberg, 2004.

[34] P. R. Spalart, S. Deck, M. L. Shur, K. D. Squires, M. K. Strelets, and A. Travin, "A new version of detached-eddy simulation, resistant to ambiguous grid densities," *Theoretical and Computational Fluid Dynamics*, vol. 20, no. 3, pp. 181–195, 2006.